Unravelling CO oxidation reaction kinetics on single Pd nanoparticles in nanoconfinement using a nanofluidic reactor and DSMC simulations

Chemical Engineering Science: X 9 (2021) 100088

Contents lists available at ScienceDirect

Chemical Engineering Science: X

journal homepage: www.elsevier.com/locate/cesx

Unravelling CO oxidation reaction kinetics on single Pd nanoparticles in nanoconfinement using a nanofluidic reactor and DSMC simulations

Sangita Swapnasrita [a], David Albinsson [b], Georg R. Pesch [c], Henrik Ström [d], Christoph Langhammer [b], Lutz Mädler [a,*]

[a] Leibniz Institute for Materials Engineering – IWT, University of Bremen, 28359 Bremen, Germany
[b] Department of Physics, Chalmers University of Technology, 412 96 Göteborg, Sweden
[c] Faculty of Production Engineering, Chemical Process Engineering, University of Bremen, 28359 Bremen, Germany
[d] Division of Fluid Dynamics, Department of Mechanics and Maritime Sciences, Chalmers University of Technology, 412 96 Göteborg, Sweden

ARTICLE INFO

Article history:
Received 24 June 2020
Received in revised form 13 October 2020
Accepted 20 January 2021

Keywords:
DSMC
Microfluidic reactor
CO oxidation
Flow simulation
Monte Carlo methods
Pd nanoparticles

ABSTRACT

Steady state catalytic oxidation of CO in nanofluidic channels decorated with Pd nano particles was studied using the Direct Simulation Monte Carlo (DSMC) method. Diffusion, collision, adsorption, desorption and reaction processes are simulated simultaneously. The influence of various adsorption (sticking coefficient, saturation coverage), desorption (activation energy, pre-exponential factor) and reaction (activation barrier) parameters on the final CO_2 turnover are determined. These effects are considered to tune DSMC surface reaction model with respect to the experimental results. With DSMC, it was possible to get insights on reactivity of the individual Pd particles and the resulting varying reaction conditions along the channel due to local conversion effects. From the local coverages, the limit of $CO:O_2$ inlet ratio to get maximum CO_2 turnover without poisoning the catalyst with CO were determined. The approach paves the way to accurately represent micro- and nanoscale flows at the same system size as that of experiments.

1. Introduction

Surface chemical reactions are a predominant part of heterogeneous catalysis, which in turn is a key part of the chemical industry including refinery processes, semiconductors development and manufacturing, fuel cell production, production of pharmaceuticals etc. With increasing computational power, numerical models have been developed to understand and predict reaction mechanisms and reaction rates especially for catalysis and reactor design (Deutschmann, 2012). They can be detailed down to individual atoms (Molecular Dynamics, MD), electrons (Density Functional Theory, DFT) or can have a reactor-scale approach (Computational Fluid Dynamics, CFD). This is the consequence of the fact that surface reactions occur across multiple scales of time and length. For example, for rarefied gas dynamics, as it happens for gas flows in mesoporous catalysts, the gas density is low such that the mean free path of the gas becomes comparable to the bounding geometry. Furthermore, while diffusion occurs in nanoseconds over micrometers, reaction can occur in picoseconds and proceed at the scale of nanometers. Hence, hardly any numerical model can handle the broad spectrum of interlaying processes without incurring enormous computational expense or compromising the accuracy of the predicted results.

On one end, DFT or MD simulations can provide very useful insight into the binding energies of atoms at the surfaces, but they neglect the engineering aspects of mass and heat transfer. On the other end, CFD simulations completely ignore the minutiae of atomic exchanges and are only focused on the macroscopic details such as mixing or mass flows. In the attempt to bridge the gap, the Kinetic Monte Carlo (kMC) and Direct Simulation Monte Carlo (DSMC) methods are designed to link the microscopic particulars with the macroscopic continuity. KMC simulations attempt to do this by stochastically predicting trajectories of the system from state to state without solving the trajectory for each individual molecule. The trajectories are then averaged over a long period of time to ensure correct evolution of the system. The algorithm chooses the stochastic states from a large database of rate constants of all the underlying processes (Andersen et al., 2019). DSMC simulations decouple the steps of mass transfer and surface interaction. While the molecules are moved deterministically, the collisions and surface mechanisms are handled stochastically. With this phenomenological approach, the DSMC algorithm gives

* Corresponding author.
E-mail address: lmaedler@iwt.uni-bremen.de (L. Mädler).

https://doi.org/10.1016/j.cesx.2021.100088
2590-1400/

Nomenclature

Acronyms

AES	Auger Electron Spectroscopy
CFD	Computational Fluid Dynamics
DFT	Density Functional Theory
DSMC	Direct Simulation Monte Carlo
kMC	Kinetic Monte Carlo
MC	Monte Carlo
MD	Molecular Dynamics
PLIF	Planar Laser-Induced Fluoroscence
PM-IRAS	Polarization Modulation Infrared Reflection Absorption Spectroscopy
STEM	Scanning Tunneling Electron Microscopy
TEM	Tunneling Electron Microscopy
UHV	Ultra-High Vacuum
VSS	Variable Soft Sphere
QMS	Quadrupole Mass Spectrometer

Symbols	**Meaning [Units]**
A_{coll}	Collision cross-section [m^2]
A_f	Area of the face [m^2]
c_r	Relative velocity between collision pair [m/s]
d	Desorption order [-]
expCO/ expO	Dependence of θ_{req} on θ [-]
E_A	Reaction activation barrier [kJ/mol]
$E_{des}(\theta)$	Desorption activation barrier at coverage θ [kJ/mol]
$E_{lateral}$	Interaction energy between nearest neighbours [kJ/mol]
k_{CO}	Fitting factor [-]
K	Adsorption prefactor [-]
n	Parcel size [-]
n_{max}	Maximum parcel size [-]
N_{ads}	Number of adsorbed molecules of a particular species [atoms]
N_C	Number of parcels in a cell [-]
N_{Pd}	Number of Pd atoms in a particular face of the solid catalyst [atoms]
p_{coll}	Probability of collision [-]
r_{des}	Desorption rate [$(atoms{\cdot}cm^{-2})^d s^{-1}$]
r_{LH}	Reaction rate [$atoms{\cdot}cm^{-2}s^{-1}$]
R	Random number [-]
R_g	Gas constant [$kJ{\cdot}K^{-1}$ $kmol^{-1}$]
S	Sticking coefficient [-]
S_0	Sticking coefficient for a clean surface [-]
t	Timestep [s]
T	temperature [K]
V	Volume of the channel [m^3]
V_C	Volume of the cell [m^3]
y_i	Volume fraction of different gas species [-]
θ	Extent of coverage [-]
θ_{req}	Vacant sites available for adsorption [-]
θ_{sat}	Maximum coverage possible [-]
σ	Surface coverage [$atoms/m^2$]
ν_A, ν_B	Constant for pre-exponential factor in desorption rate [s^{-1}]
ν_{des}	Desorption pre-exponential factor [s^{-1}]
ν_{LH}	Reaction pre-exponential factor [$cm^2/(atom{\cdot}s)$]

accurate results for scales less than the mean free path of molecules (Alexander and Garcia, 1997). DSMC has been used to simulate homogeneous reactions by means of collision (Gimelshein and Wysong, 2017; Bird, 2011). Dreyer et al. studied the diffusion of gas mixtures in porous structures (Dreyer et al., 2014). Pesch et al. added surface adsorption, desorption and reaction models to simulate CO and O_2 flow in a porous Pd structure (Pesch et al., 2015) and previous works by our group have focused on making the algorithm developed by Pesch et al. more efficient by reducing the computational time (Swapnasrita et al., 2019). The mean field approximation is used to assume a uniform surface neglecting surface defects, edges etc.

Another important aspect is the origin of the used input parameters in numerical simulations. KMC rate constants are primarily linked to first principles calculated energies (Andersen et al., 2019; Rogal et al., 2007). The surface and molecular data for DSMC simulations are taken from computations (Pan et al., 2019) and experiments (Swaminathan-Gopalan et al., 2018; Swaminathan-Gopalan and Stephani, 2019), which creates a natural direct link between experiment and simulation. In this regard, the strength of DSMC simulations also lies in coupling the transport and kinetics of the reactor systems and at the scale of the reactor itself. While most of the numerical simulations would require a representative volume element and extrapolate the data to the entire domain, DSMC is capable of simulating non-continuum flows in the entire reactor, while preserving the kinetics and transport parameters at a molecular level. Furthermore, when the reactor geometry is complex, as for a porous medium with winding pores, interconnected cavities, dead ends and surface defects characteristic for real catalyst materials, DSMC is a well-validated and powerful tool to extract transport and adsorption, desorption and reaction parameters. Nevertheless, care must be taken when transport phenomena and chemical kinetics are closely coupled and conventional continuum descriptions break down, to avoid misinterpretation of key phenomena especially when the individual steps of the DSMC framework are insufficiently validated.

Here, we focus on investigating the performance of a reactive DSMC framework in predicting the behavior of a heterogenous catalytic system – CO oxidation over single Pd nanoparticles–in a well-defined nanoreactor geometry. The specifically designed nanoreactor system is small enough to be directly simulated and thus enables a unique direct comparison between the experiment and simulation. The primary ambition is to establish under what circumstances the reactive DSMC framework can provide accurate descriptions of the system behavior. The surface reaction algorithm utilizes a mean field approach to model individual chemical processes on the gas-catalyst interface. Furthermore, we further explore how the richness of data available from the DSMC simulation can help elucidate aspects of the system behavior that are difficult to be characterized in experiments alone. As the key result, it is found that DSMC is able to provide specific particle kinetics while conserving the diffusion data in the complete reactor as well. Exhaustive sensitivity studies are performed to find the important simulation parameters and the parameters are varied in the simulation model to match the experimental data. The kinetic parameters found after fitting are well within experimental bounds and can be explained with help from literature. However, it should be noted that this set of parameters is applicable only to this particular reactor and any new reactor system can be handled in a similar way to find its own unique set of parameters.

2. Experimental setup

We utilize a newly developed *nanoreactor* platform (Albinsson et al., 2020) that allows us to make catalytic model reactors with reactor volumes in the 10^{-15} to 10^{-12} L range and overall reactor

dimensions directly accessible to DSMC simulations. In brief, the nanoreactor chip is made by etching nano-/microfluidic channels in a Si/SiO_2 chip (Fig. 1(a)) following a series of nanofabrication steps that are explained in detail elsewhere (Albinsson et al., 2020). The particles were fabricated by electron beam deposition and annealing at 550 °C in Ar. The chip comprises two separate microfluidic systems that are connected to an array of mass flow controllers (MFCs) and a pressure controller on the inlet side; and to a vacuum chamber equipped with a quadrupole mass spectrometer (QMS) on the outlet side (Fig. 1(a)). This enables reaction conditions (gas composition and pressure) to be defined on the inlet side and reaction products to be measured at the outlet. Towards the "tip" of the chip, the microfluidic systems are connected to a nanofluidic system that contains the catalyst bed (Fig. 1(b)-(c)). The nanofluidic system has a U-shaped design with a central region comprised of 40 identical parallel nanochannels (each 100 μm long, 100 nm high and 500 nm wide) that act as the reactor (Fig. 1(d)-(e)). Each channel is decorated with 18 nominally identical Pd nanoparticles (100 nm in diameter, 40 nm in height) generated with an electron beam evaporation through a deposition mask made using electron beam lithography (Fig. 1(e)-(g)). The deposited particles are polycrystalline in nature. Alekseeva et al. have shown grain boundaries for different material produced by the same method (Alekseeva et al., 2017). A single channel is small enough to be simulated by DSMC and by having 40 parallel channels, the total flow through the system is high enough to enable efficient measurements of reaction products by mass spectrometry. A Pt-based thin film heater placed on the back of the chip enables temperature control of the reactor via a PID (Lakeshore 335). Flow through the nanochannels is achieved with a high pressure (1–5 bar) on the inlet side, and pumping the outlet side to UHV conditions ($<10^{-9}$ mbar).

Experiments were conducted with an inlet pressure of 2 bar, resulting in a pressure of 1 bar at the catalyst bed (Albinsson et al., 2020) and at three temperatures (498, 523 and 548 K). For each temperature, the O_2 concentration was held constant at 6%, while varying the CO concentration from 0.2 to 4% in steps (example shown in Figure S3 in the SI). Ar was used as an inert carrier gas. The catalytic activity was measured monitoring the reaction products CO_2, CO and O_2 (m/z = 44, 28 and 32, respectively) at the outlet of the reactor. The QMS measures the gas concentration in intervals of 10 s and a mass balance has been performed to calibrate the readout. Prior to each experiment, a cleaning procedure was conducted exposing the reactor to 5% O_2 in Ar at 673 K for 30 min.

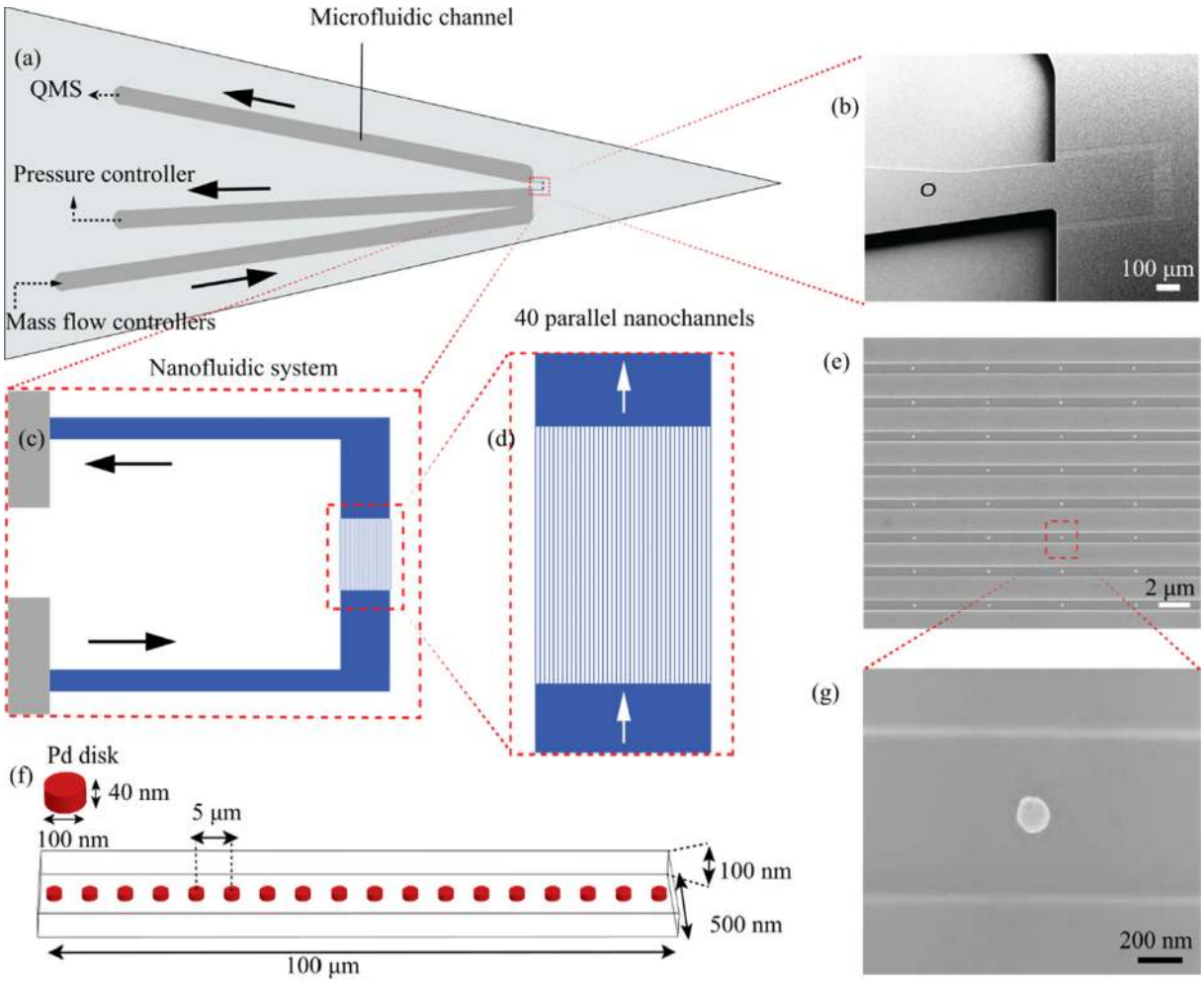

Fig. 1. (a) Schematic of the nanoreactor chip, illustrating the microfluidic channels that connect the inlet side to an array of MFC's and a pressure controller, and the outlet side to a QMS. (b-c) SEM image (b) and schematic illustration (c) of the nanofluidic system that connects the two microfluidic channels. (d) Zoomed in view of the model catalyst bed comprised of 40 identical nanochannels, each containing 18 cylinder-shaped Pd nanoparticles with 100 nm diameter and 40 nm height. (e) SEM image of parallel nanochannels decorated with Pd nanoparticles. (f) Schematic illustration of a single nanochannel with disk-shaped Pd nanoparticles (red) placed 5 μm apart. (g) SEM image of a single Pd nanoparticle inside a nanofluidic channel. (For interpretation of the references to colour in this figure legend, the reader is referred to the web version of this article.)

3. Simulation setup

It is assumed that the 40 parallel nanochannels studied in the experiment have similar activity, since they are nominally identical. Thus, to save computational time, only one channel is simulated and CO_2 concentration is calculated only at the outlet. Using the blockMesh mesh generator in OpenFOAM (Scanlon, 2010; Roohi and Stefanov, 2016), an empty cuboid mesh with cells of 10 nm cubic dimensions is generated. Then the mesh generation utility SnappyHexMesh is used to setup the cylindrical particle. These are the only active substance in the entire simulation domain. The generated mesh is shown in Fig. 2. The surface is assumed to be single Pd(1 1 1) crystal and the lattice parameters are taken from Engel and Ertl (Engel and Ertl, 1978). Since the chip temperature is completely controlled with a Pt heater, the simulation parameters are set to purely isothermal and energy conservation is neglected. The algorithm used in this work is based on Pesch's model for surface chemical reactions using DSMC (Pesch et al., 2015). The simulations are conducted on a single node with 24 Intel Xeon Gold 6136 3.00 GHz cores.

3.1. Inflow

The initial number densities of the gases are,

$$\rho_i = \frac{y_i V}{p R_g T} \tag{1}$$

where $y_i$is the mole fraction of the gas components, V is the volume of one channel, p refers the pressure which is 1 atm, R_g is the gas constant and T represents the uniform temperature maintained on the chip. Inlet CO concentration is varied between 0.05 and 3 %, O_2 concentration is constant at 6% and while the rest is Ar. The gas molecules are grouped into parcels of varying sizes (see Fig. 3). We would like to note here that parcels are known in the DSMC community as "simulator particles" and each simulator particle represents F_{num} number of real molecules. However, to avoid any confusion between the catalyst particles and the gas molecules, henceforth, we refer to the catalyst as "particle", gas particles as "parcels" and F_{num} as "parcel sizes". The parcel sizes (the number of molecules represented by a parcel) may vary from 1 to a maximum size, specified by the user at the beginning. Flow is directed towards the outlet by maintaining a pressure difference between the inlet and outlet. When the parcel collides with the surface, the molecules belonging to the parcel then engage in adsorption. The adsorption probability for all molecules is calculated independently depending on the surface coverage and sticking coefficients. The adsorbed molecules can then desorb or react depending on the individual probabilities given by equations (10)

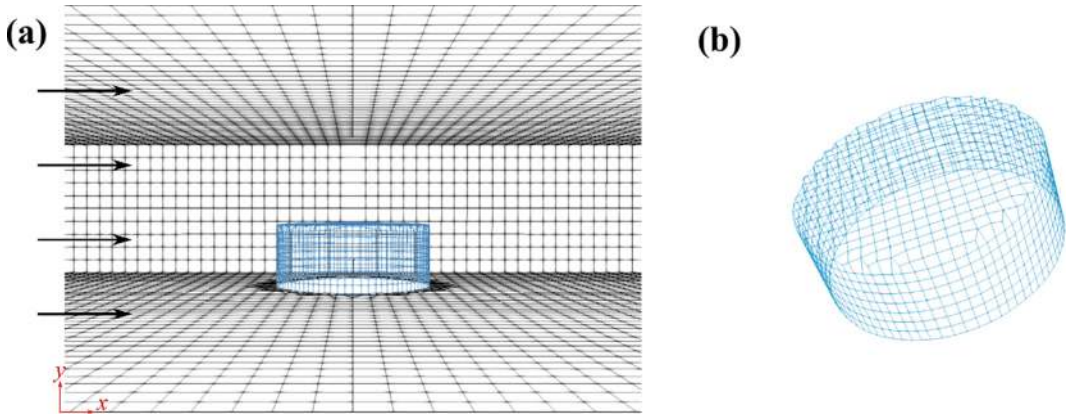

Fig. 2. Computational mesh of the setup. The setup has dimensions: 78 μm × 100 nm × 500 nm. The entire setup is divided into computational cells of 10 nm × 10 nm × 10 nm. The dimensions have been reduced at the inlet and outlet to avoid simulating the extra inlet and outlet spaces. A steady flow is assumed in the whole system and the boundary condition at the inlet has been fixed as such. In this setup, each cell has 10 nm cubic dimension. According to the experimental system, there are 18 cylindrical Pd particle in series, while each Pd particle has a height of 40 nm and a diameter of 100 nm. (a) *xy* cross-section of the domain. (b) The cylindrical Pd particle.

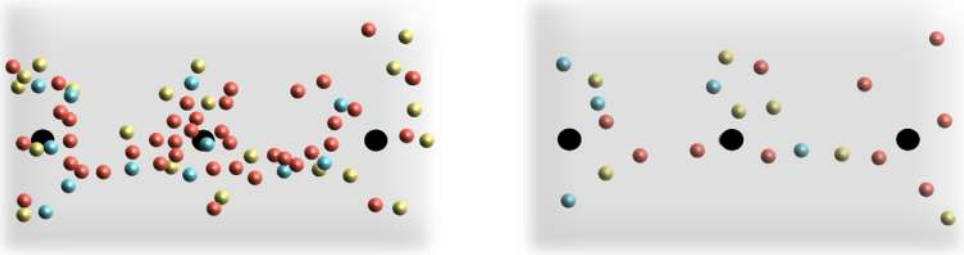

Fig. 3. The implementation of parcel method. A section of the nano channel is shown here (top view), black circles representing the active Pd particles. Different colored spheres represent the three species of molecule initialised, CO, O_2 and Ar. In (a), each real molecule is represented by a single simulated molecule whereas in (b), each simulated molecule could represent any number of molecules, referred to as *parcel size* henceforth, from 1 to n_{max} (where n_{max} is user-specified during initialisation). This reduces the computational time following the individual trajectories. (Blue: CO; Yellow: O_2; Red: Ar). (For interpretation of the references to colour in this figure legend, the reader is referred to the web version of this article.)

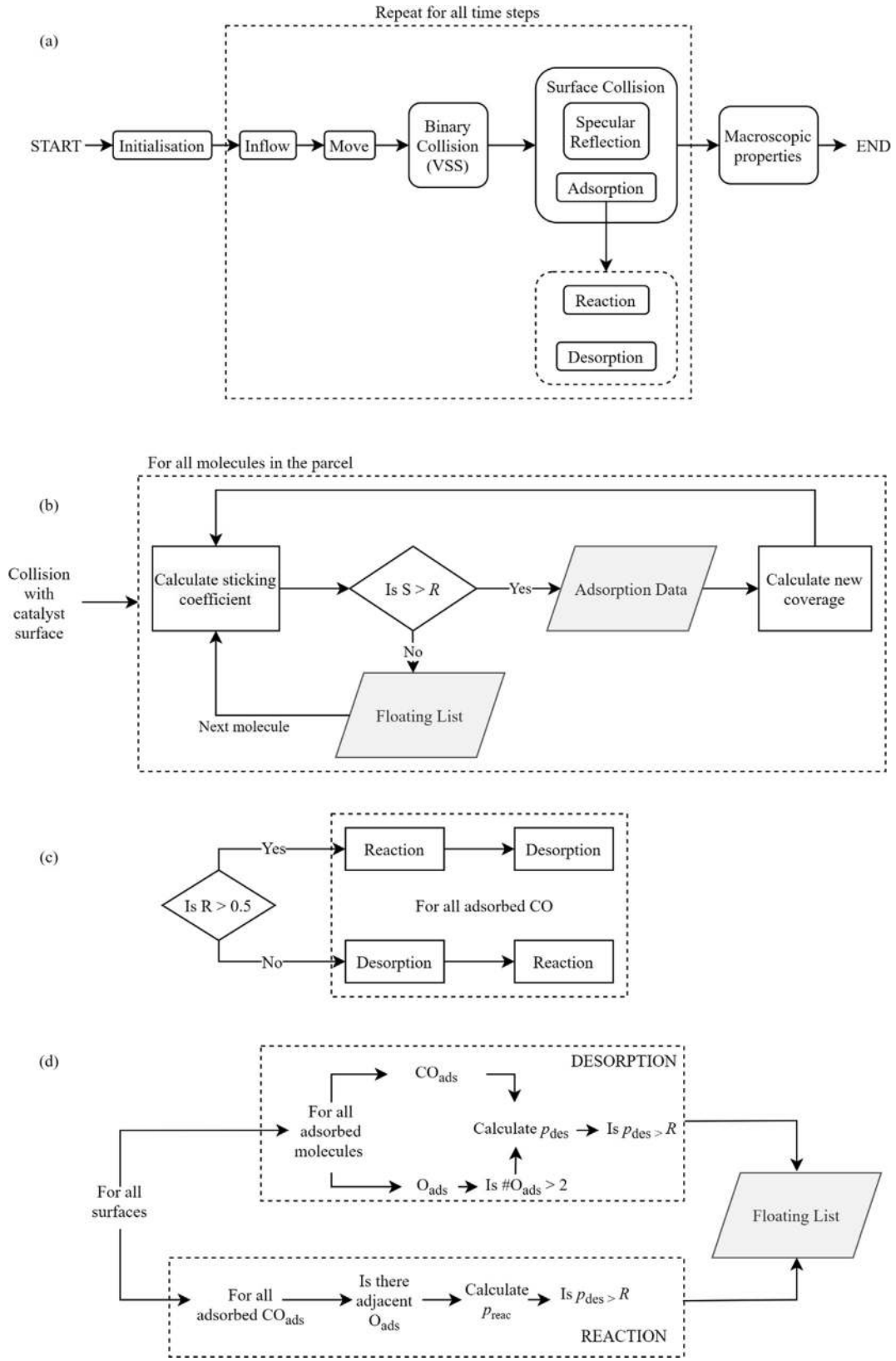

Fig. 4. (a) A complete schematic of the DSMC simulation extended for surface reactions. (b) Adsorption algorithm used in the model. The desorption or reaction step follows the adsorption step. The order of implementation is decided by a random number (c). (d) Reaction and desorption sub-routines.

Table 1
All input parameters of the simulations.

Input parameters	CO	O_2
Concentration of CO and O at inlet	0.05 – 3%	6%
Parcel Size, n_{max}	50	
θ_{sat}	0.33	0.25
Lattice constant	2.74 Å	
Temperature	498 – 548 K	
Adsorption constants (taken from Kisliuk precursor model (Kisliuk, 1957; Kisliuk, 1958)		
S_0	1	0.60
K	0.15	0.71
Desorption constants (taken from Polanyi-Wigner theory (Kolasinski, 2012; Guo and Yates, 1989; Guo et al., 1989		
$E_{des}(0)$ (kJ/mol)	147	222
$E_{lateral}$ (kJ/mol)	−153	−69.6
ν_A	16	−1.7
ν_B	−15	0
Reaction constant		
Langmuir-Hinshelwood mechanism	83.68	
E_A (kJ/mol) (Creighton et al., 1981)		

and (13). A variable parcel simulation algorithm has been used throughout this paper (Fig. 4) and the simulation parameters, indicated in table 1 are manipulated to see the effect on the predicted results.

3.2. Collision

Collisions between parcels are only sampled if they are present in the same computational subcell independent of their position (Roohi and Stefanov, 2016). The collision sampling between parcels is performed assigning random probabilities to collision pairs dependent on the size of the parcels and the collision cross-section. The collision cross-section is calculated using the variable soft sphere (VSS) model, which takes into account the viscosity and momentum dependence of cross-section during collisions (Koura and Matsumoto, 1992). After comparing this probability to a random number, the parcels are assigned post-collision velocities. This method is also known as no-time counter (NTC) method (Bird and Brady, 1994). It is time efficient as it allows for prior selection of collision partners. It should be noted that there are other collision models available such as

Simplified Bernoulli Trial (SBT) (Amiri-Jaghargh et al., 2014) and Generalised Bernoulli Trial (GBT) (Roohi et al., 2018). In case of collision between like molecules, there is a parcel agglomeration if the net number of molecules between the two is less than n_{max}. The collision schematic is shown in Fig. 5. When the parcel collides with the surface, it can specularly reflect from the surface without any change to the tangential velocity and a complete reversal of the normal velocity. However, if the sticking coefficient of the surface is sufficient, the parcel may adsorb on the surface. Since adsorption, desorption and reaction processes are collectively known as "reactions", the terms are kept separate for clarity. The full schematic of the DSMC surface solver is shown in Fig. 6.

3.3. Adsorption model

When a parcel collides with a surface, all molecules of the parcel can adsorb on the surface depending on the coverage and the sticking probability (Fig. 4b). The adsorption model is based on Kisliuk's precursor model (Kisliuk, 1957; Kisliuk, 1958). The coverage of the adsorbed species is determined by

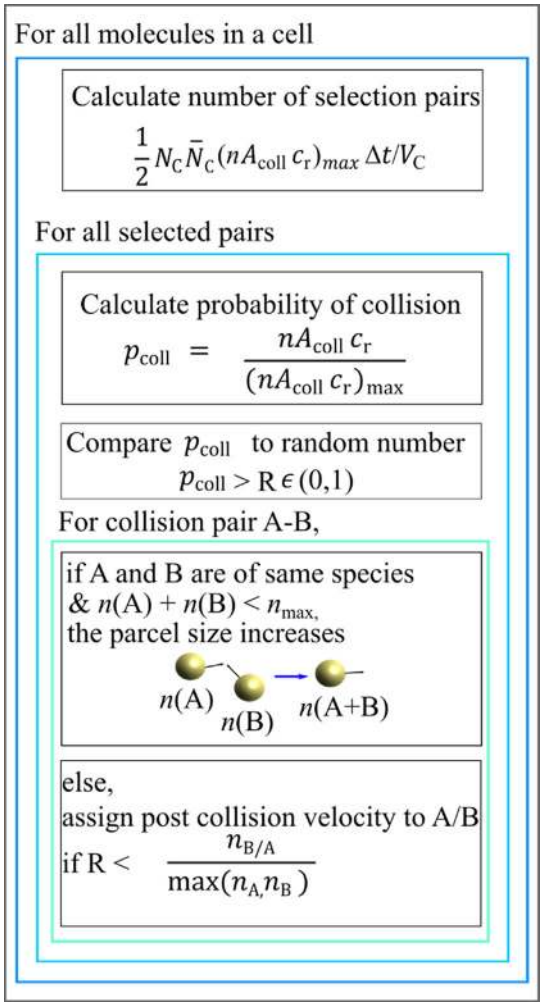

Fig. 5. Collision sampling process in a variable parcel size DSMC algorithm. N_C number of parcels in the cell, V_C volume of the cell, n parcel size, A_{coll} collision cross-section, c_r relative velocity between the collision pair and p_{coll} probability of collision. R is a uniformly distributed random number between 0 and 1.

$$\theta = \frac{N_{ads}}{\theta_{sat} \cdot N_{Pd}} \tag{2}$$

where N_{ads} is the number of adsorbed molecules and $\theta_{sat} \cdot N_{Pd}$ gives the number of maximum number of adsorbed molecules of that species. The saturation coverage of CO and O are 0.33 and 0.25, respectively (Engel and Ertl, 1978). CO is molecularly adsorbed on the Pd lattice (*expCO* = 1). The number of vacant sites for CO is determined by

$$\theta_{req,CO} = (1 - \theta_{CO})^{expCO}. \tag{3}$$

The adsorption of CO is unhindered by O while O adsorption is inhibited by adsorbed CO. However, O coverage is completely inhibited if CO coverage is greater than 0.33. To account for this difference in the adsorption of O and CO, the coverage of O also includes the coverage of CO. It is assumed here that the dependence is completely linear.

$$\theta_O = \theta_{CO,current} + \theta_{O,current} \tag{4}$$

$$\theta_{req,O} = (1 - \theta_O)^{expO} \tag{5}$$

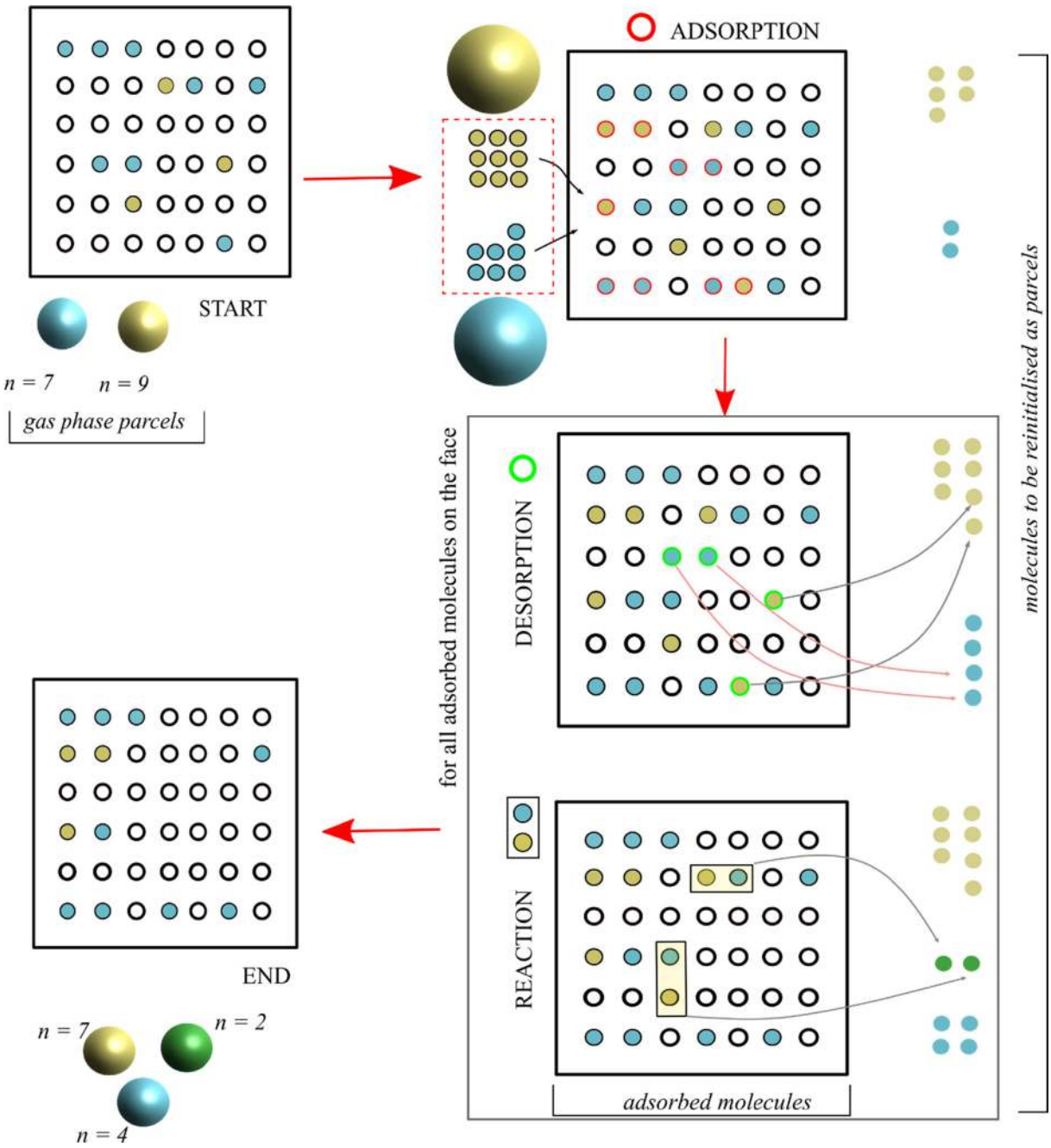

Fig. 6. Representation of all the surface mechanisms in the DSMC algorithm. The gas phase molecules may adsorb on the surface upon collision. The red dashed rectangle (in the adsorption step) shows the molecules included in the gas-phase parcel that collides with the surface. For all the adsorbed molecules, the reaction and desorption routine is implemented once each. All the molecules desorbed from the surface (molecules shown on right-hand side) are then grouped into a parcel and initialised to the gas phase in the same time step. This process is repeated for all the faces of the solid catalyst. Parcels are shown as 3D spheres with gradients and molecules are shown as flat circles. The filled circles on the surface with thin outlines are adsorbed molecules, empty circles are vacant sites, and filled circles without outlines (shown to the right of the surface) are to be added to the gas phase at the end of the time step. (Blue: CO; Yellow: O_2; Green: CO_2. Ar is inert to surface adsorption. The numbers shown here are examples.) (For interpretation of the references to colour in this figure legend, the reader is referred to the web version of this article.)

Every molecule of O_2 requires two adjacent spots to adsorb dissociatively. So, *expO* is usually taken as 2. The sticking probability is then calculated from θ_{req} for each molecule that hits the solid surface,

$$S = \frac{S_0}{1 + K\left(1/\theta_{req} - 1\right)} \tag{6}$$

where S_0 is the sticking probability on a clean surface and K is the prefactor. The molecules that are unadsorbed are added to a *floating list* and the molecules from this list are initialised into the gas phase at the end of each time step. After adsorption is completed for all faces of the solid surface, a uniformly distributed random-number is compared to 0.5 to decide which of the reaction or desorption routine is implemented first (Fig. 4c). Surface diffusion processes are neglected in the simulation and individual modeling of molecules on the surface is neglected following the mean field approximation.

3.4. Desorption model

The desorption of CO and O_2 is based on Polanyi-Wigner model (Kolasinski, 2012). CO molecularly desorbs from the surface and O

undergoes associative desorption. The desorption algorithm is shown in Fig. 4d. The desorption activation energy is dependent on the coverage θ and the lateral interactions between the nearest neighbours of the same species, E_{lateral}, which includes the association barrier for O_2 desorption.

$$E_{\text{des}}(\theta) = E_{\text{des}}(0) + E_{\text{lateral}}\theta \tag{7}$$

The desorption rate is then given by,

$$r_{\text{des}} = \nu_{\text{des}}\sigma^d \exp\left(\frac{-E_{\text{des}}}{R_g T}\right) \tag{8}$$

where ν_{des} is the pre-exponential factor, d is the desorption order (1 for CO and 2 for O_2), σ is the surface coverage given by the ratio N_{ads}/A_f, A_f being the area of the face of the solid catalyst, R_g is the universal gas constant and T is the temperature of the system. The pre-exponential factor is also dependent on the coverage, where ν_A, ν_B are constants.

$$\nu_{\text{des}} = 10^{\nu_A + \theta\nu_B} \tag{9}$$

The desorption probability is given by

$$p_{\text{des}} = \frac{r_{\text{des}}\Delta t}{\text{N}_{\text{ads},i}}. \tag{10}$$

where Δt is the time step and $N_{\text{ads},i}$ is the number of adsorbed molecule of species i on the particular surface.

3.5. Reaction model

It is general accepted that CO oxidation on Pd follows the Langmuir-Hinshelwood mechanism (Engel and Ertl, 1978; Engel and Ertl, 1978; Engel and Ertl, 1979; Conrad et al., 1978; Berlowitz et al., 1988; Hendriksen, 2004). A mean field second-order rate equation is used that depends on the surface concentrations. According to the mechanism, adsorbed CO and adsorbed O molecules react to form one molecule of CO_2, which after desorption leaves behind two vacant sites ($*$). The desorbed CO_2 is added directly to the *floating list.*

$$\text{CO}(g) + * \Longleftrightarrow \text{CO}_{\text{ads}}$$

$$\text{O}_2(g) + 2* \Longleftrightarrow 2\text{O}_{\text{ads}}$$

$$\text{CO}_{\text{ads}} + \text{O}_{\text{ads}} \Rightarrow \text{CO}_2(g) + 2* \tag{11}$$

The reaction rate is given by the pre-exponential factor, the surface coverage of CO and O and the activation energy E_A.

$$r_{\text{LH}} = \nu_{\text{LH}}\sigma_{\text{CO}}\sigma_{\text{O}} \exp\left(-\frac{E_A}{R_g T}\right) \tag{12}$$

The desorption of CO_2 is instantaneous (Engel and Ertl, 1978; Kolasinski, 2012; Conrad et al., 1978) and is thus neglected in the desorption routine.

The molecules react based on the probability given by

$$p_{\text{reac}} = \frac{r_{\text{LH}}\Delta t}{\text{N}_{\text{ads,CO}}} \tag{13}$$

where Δt is the time step and $N_{\text{ads,CO}}$ is the number of adsorbed CO molecule on the particular surface.

3.6. Parcel initialisation

All the molecules that are desorbed from the surface, be it reactants or products are initialised into the gas phase. The parcel sizes are kept as large as possible to keep the parcel number density to a minimum. This initialisation step is necessary to maintain the local species concentration.

The surface reaction model developed for this paper is formulated to understand the fundamentals of the interplay between the chemical kinetics and mass transfer at different scales. However, other relevant mechanisms such as surface diffusion and reaction thermodynamics have been excluded at present for simplicity. Gas phase recombinations are also neglected as the reaction between CO and O_2 are hindered by a large energy barrier in the gas phase (Rogal et al., 2007).

4. Results and discussion

A benchmark test is chosen to test the performance of the surface reaction algorithm. In the corresponding experiment, a mixture of CO, O_2 and Ar is fed through the inlet of the nanoreactor. The temperature is maintained at 498 K. For varying CO concentration, a peak in CO_2 production is then observed by the QMS, reaching almost 90% conversion at 0.6% CO concentration in the feed (Fig. 7). For the corresponding simulation, the inlet CO number density is varied according to the different experimental CO concentration using Equation (1). The CO_2 concentration shown in the plot is an average of the concentration at the outlet boundary over time at a steady state. The values of the parameters used in this simulation run are given in table 1 and were adapted from the literature for CO oxidation on single crystal Pd(1 1 1). It is noted that many of these values are obtained under ultra-high vacuum (UHV) conditions while the simulation and experiment are run at atmospheric pressures and thus, this set of parameters might be non-transferrable. It is also important to note that all kinetic parameters (including activation energy, E_A) vary a lot from surface structure to surface structure and pressure and temperature regimes. Therefore, it is intended to perform sensitivity studies to determine which parameters are important and then vary the parameters to match the experimental results.

It is clearly seen in Fig. 7 that the predicted CO_2 concentration is at least one order of magnitude smaller than the experimental values. A clear peak in the CO_2 production is seen in the experimental data resulting from the poisoning of the surface by CO with increasing CO concentration. This is in agreement with the observations from Engel and Ertl (Engel and Ertl, 1978; Engel and Ertl,

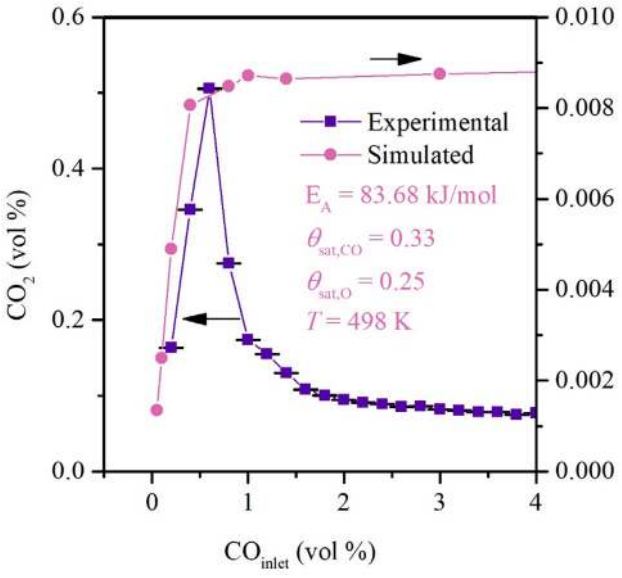

Fig. 7. The experimental and the simulated CO_2 concentration data is plotted against the feed CO concentration at T = 498 K plotted with the parameters from table 1. The simulated data are one order of magnitude smaller than the experimental data.

1978). Conversely, there is hardly any noticeable peak-like behavior observed in the simulated concentrations. This discrepancy between the simulation and experiment raises the following questions:

1. How different are the parameters considered in the simulations (table 1) from the actual experimental values? What is the impact of the simulation input parameters on the predicted CO_2 concentration?
2. What kind of lattice structure is formed when the Pd is added into the nanochannels? What is the effect on the reaction mechanism?
3. The volume-averaged reaction rate generally increases with temperature and so does the desorption rate. How would an increase in temperature affect the effective reaction rate, knowing that it is largely dependent on the surface CO? Can the algorithm be used to predict CO_2 concentrations at higher temperatures?

The answers to these questions are explored in the following sections. To answer the first one, a thorough sensitivity test is conducted with multiple simulation parameters from the simulation to better reflect the experimental behavior. This includes adsorption parameters: saturation coverages $\theta_{sat,CO}$, $\theta_{sat,O}$; initial sticking probabilities $S_0(CO)$, S_0 (O); and dependence of sticking probability on existing coverage *expCO* and *expO*. The desorption parameters: desorption energy at zero coverage $E_{des}(0)$, lateral interaction barrier $E_{lateral}$ and pre-exponential constants υ_A and υ_B are also checked. All these parameters already have an effect on the CO_2 production rate as seen in later figures. Additionally, the reaction rate is also very much dependent on the reaction activation barrier, E_A and thus it was included in the sensitivity study. From these studies, predictions can be made regarding surface characteristics such as surface coverage, the reaction kinetics, and the relation between the transport and reaction mechanisms that the experiments are unable to provide independently.

In Fig. 8(a), the predicted CO_2 concentration is increased by an order of magnitude varying the reaction activation energy between 83.68 and 10.0 kJ/mol. This is the consequence of the Langmuir-Hinshelwood mechanism and the corresponding exponential dependence of the reaction rate on the activation energy. It follows from equation (11), that, if the activation energy is reduced, the reaction rate increases as

$$\frac{r_2}{r_1} = \exp\left[\frac{-(E_{A,2} - E_{A,1})}{T}\right] \tag{14}$$

However, in the reaction system at hand, the CO_2 production rate is not only dependent on the kinetics of the rate determining step of the surface reaction, but also on mass transport such as the diffusion rate of the reactants in the gas phase. Specifically for a lower activation energy, the reaction quickly becomes mass transfer-limited due to the faster turnover rate in the surface reaction. For this system, it is observed that below 40 kJ/mol the reaction has entered into a mass transfer-limited regime (see figure S5). With higher $\theta_{sat,CO}$ (blue line), the reaction rate is higher but approaches the same value as with lower $\theta_{sat,CO}$(green line) as it transitions from a kinetically limited regime to the mass transfer-limited regime.

In Fig. 8(b) and (c), the saturation coverages of CO and O are varied to investigate the influence on the predicted CO_2 concentration at the reactor outlet. This parameter defines the extent to which a surface can be covered by CO or O. Literature suggests CO is dom-

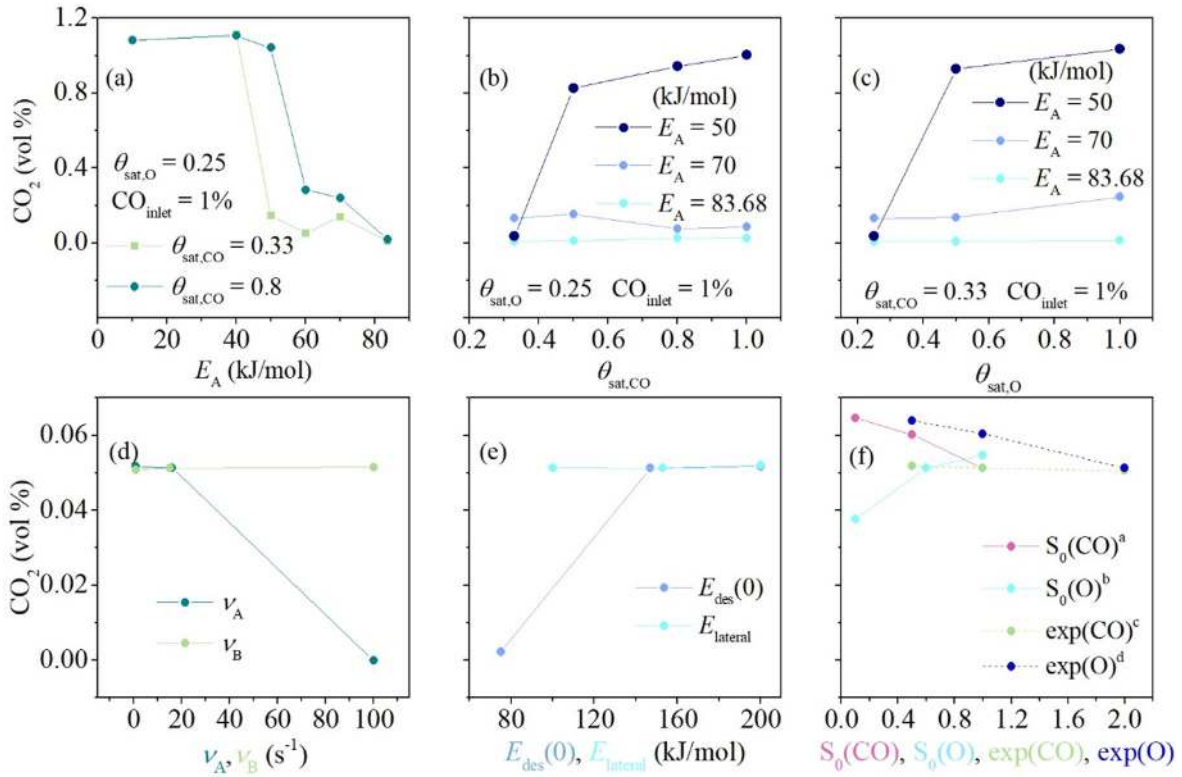

Fig. 8. Concentration of CO_2 at the outlet as (a) reaction activation energy, E_A is decreased from a literature value of 83.68 kJ/mol (Creighton et al., 1981) to 10.0 kJ/mol, (b) the saturation coverage for CO is increased from 0.33 (literature, (Engel and Ertl, 1978) to 1. The saturation coverage for O is maintained at 0.25, (c) the saturation coverage for O is increased from 0.25 (literature, (Engel and Ertl, 1978) to 1, keeping the rest of the parameters constant. The saturation coverage for CO is maintained at 0.33, (d) & (e) the parameters of desorption model are varied and (f) the adsorption parameters of the adsorption model are varied to see the influence on the CO_2 production. [a] S_0 (O) = 0.6, exp (CO) = 1.0, exp(O) = 2.0, [b] S_0 (CO) = 1.0, exp(CO) = 1.0, exp(O) = 2.0, [c] S_0 (CO) = 1.0, S_0 (O) = 0.6, exp(O) = 2.0, [d] S_0 (CO) = 1.0, S_0 (O) = 0.6, exp(CO) = 1.0.

inantly adsorbed on Pd surface and can replace adsorbed O atoms, even if the surface is saturated with O and the effect of this behavior is observed to reduce upon increasing temperature. For the simulations, the inlet CO concentration is kept constant at 1% and $\theta_{sat,CO}$ and $\theta_{sat,O}$ values are increased. Based on a linear fitting for E_A = 83.68 kJ/mol, the CO_2 concentration increases with a slope of 0.02 (R^2 = 0.91). This implies that the CO_2 production is unaffected by saturation coverage. However, with a lower activation barrier, the CO adsorbed on the surface can react more easily. When the reaction rate is competitive enough with the adsorption rate, the CO_2 production rate will be higher. Thus, at a lower reaction activation energy, the CO_2 production can be increased with reduction in CO saturation coverage.

In Fig. 8(d) and (e), the parameters belonging to the Polanyi-Wigner desorption model are varied and the corresponding effect on the CO_2 production rate is studied. To increase the reaction rate, some of the adsorbed CO needs to be desorbed from the surface to create vacant sites for O adsorption. Thus, only the parameters pertaining to CO desorption are investigated to see its effect. The two main parameters in this model are the activation barrier and the pre-exponential factor, both of which are in turn dependent on coverage. By lowering the activation energy and increasing the pre-exponential factor, one can increase the reaction rate. The following conclusions are drawn from this section:

- With increasing activation barrier, CO is able to stay on the surface longer and the reaction rate is higher. The reaction rate decreases to almost zero as $E_{des}(0)$ is reduced and the adsorbed CO concentration reduces.
- The reaction rate is independent of any changes in $E_{lateral}$.
- The reaction rate reduces with v_A and remains unaffected by v_B.

In Fig. 8(f), the parameters of the Kisliuk adsorption model, described in section 3.3, are studied. According to Guo et al., the sticking coefficient of CO on a clean surface and the prefactor are fixed at 1.0 and 0.71 irrespective of temperature (Guo and Yates, 1989). Hence, CO will almost certainly adsorb on the surface. Reducing the CO sticking probability would allow for more O to adsorb. A similar effect is also achieved if the sticking probability for O_2 were to be increased. It is expected that the reaction rate would increase if S_0(CO) is reduced and S_0(O) is increased. The other parameter that is under consideration is the power dependence on the existing coverage. As shown in equations (3), 5 and 6, the sticking probability is inversely dependent on the existing coverages. This coverage is then raised to a power of 1 for molecular adsorption of CO and 2 for dissociative adsorption of O_2. Varying these exponents will influence the sticking coefficient and in turn the surface coverages. From the Fig. 8(f), it is seen that:

- With reducing CO initial sticking coefficient, the reaction rate increases as the number of vacant sites for O adsorption increases.
- With increasing O initial sticking coefficient, the reaction rate increases as the probability of O adsorption goes up.
- The CO coverage is already saturated at this inlet CO composition. Also, the CO coverage depends only on sites filled by CO. Thus, the reaction rate remains almost unchanged despite increasing *expCO*.
- With increasing *expO*, the dependence on the filled sites increases. Therefore, the reaction rate decreases.

Comparing the results from Fig. 8, it can be noted that the sensitivity towards changing the simulation parameters on the CO_2 output is in the following order: E_A> $\theta_{sat,CO}$ = $\theta_{sat,O}$ > $E_{des}(0)$ > v_A > *expO* = S_0 (CO) = S_0(O) (Supplementary figure S2). The other parameters *expCO*, $E_{lateral}$ and v_B have insignificant influence on the predicted concentrations. Using this information, the three parameters that were chosen to match the simulation and experimental results are the reaction activation energy E_A, the saturated CO coverage, $\theta_{sat,CO}$ and the saturated O coverage, $\theta_{sat,O}$. From the experimental data shown in Fig. 7, it is clear that the CO_2 production needs to be one order of magnitude higher and there is CO poisoning at higher inlet CO concentration. Summarising the sensitivity study, it can be concluded that,

- Reduction in E_A increases the reaction rate.
- Reducing $\theta_{sat,CO}$ at a lower E_A increases reaction rate.
- Reducing $\theta_{sat,O}$ at a lower E_A results in lower CO_2 production.

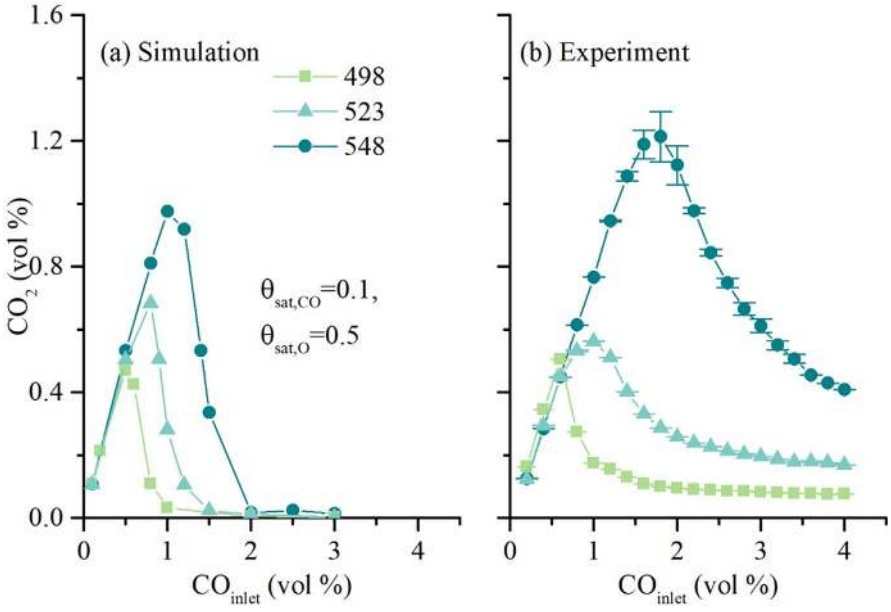

Fig. 9. Comparison of the experimental and the simulation values. The inlet CO concentration is varied from 0.05% to 4%, O_2 is constant at 6% and the rest is Ar. The activation energy of the reaction is fixed at 50 kJ/mol. The saturation coverages for CO and O are maintained at 0.1 and 0.5, respectively.

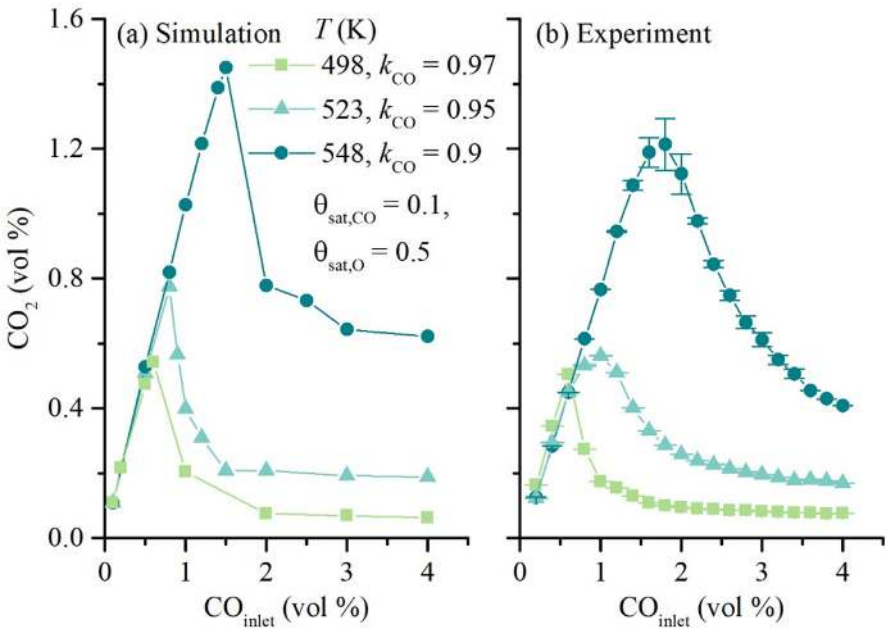

Fig. 10. Predicted CO_2 concentration by simulation in comparison with the experimental values after adding k_{CO}. Along with the parameters in Fig. 9, an additional coefficient reflecting the degree of inhibition of CO coverage on O coverage, k_{CO} is added as given by equation (12). The values shown here for k_{CO} provide the best match for the experimental data.

Thus several combinations of these three variables were studied (Supplementary) and the best match with the experimental data was obtained for $\theta_{sat,CO}$ = 0.1, $\theta_{sat,O}$ = 0.5 and E_A = 50 kJ/mol (Fig. 9). Other combinations of input parameters are also studied. The above combination showed a definitive pattern on the CO_2 concentration output. The fitting approach used here does not compromise the model and results. Although there might be more fitting approaches to obtaining the kinetic parameters, a simple optimization of the target value delivered sufficiently accurate parameters that are within reasonable bounds observed in the nanoreactor experiments:

- There is CO poisoning at higher inlet CO concentrations if the O_2 inlet rate is kept constant.
- The peak of CO_2 output occurs at higher CO concentrations for higher temperatures since the desorption rate of CO is higher.
- The reaction rate is very similar at low inlet CO concentration for all temperatures. This is because in this regime the rate is mass transfer-limited for low CO % and thus, irrespective of temperature the average amount of CO_2 produced is similar.

There are also certain features that the simulations are unable to predict, such as the position and magnitude of the CO_2 peak and overall higher CO_2 production rate at higher CO_{inlet} concentration. The predicted concentration values fall within the range seen in the experiments. In the simulation model, despite the higher reaction rate and desorption rate at higher temperatures, the surface is completely saturated by CO and O adsorption is completely inhibited. Thus the reaction rate drops to zero for all temperatures at high CO concentration. At this temperature, there is hardly any desorbed O_2 noticed in the simulation. It shows that the observed low reaction rate is due to lower availability of adsorbed oxygen rather than faster desorption of O. As a result, it can also be stated that O adsorption inhibition is primarily due to the saturated coverage of CO. In equation (4), it is assumed the number of vacant sites available for O_2 has a linear dependence on the current CO and O coverage. From the experiments, it is seen that at higher temperatures the turnover is higher, which means that the adsorption inhibition effect reduces. It is clear from Fig. 9(b) that the inhibition effect has a coefficient based on the temperature. Therefore, an additional coefficient is introduced to equation (4) to reflect this behavior in Fig. 10.

$$\theta_O = k_{CO}\theta_{CO,current} + \theta_{O,current} \quad (15)$$

The coefficient $k_{CO} = 1$ refers to a complete inhibition of O adsorption by adsorbed CO which is what was considered earlier. With temperature, the value of k_{CO} would decrease. The extreme case on the other side would be k_{CO} = 0, which means CO and O adsorb on the surface independently. In Fig. 10, the CO_2 concentration is predicted for different k_{CO} and the best fits at different temperature are shown. The value of k_{CO} is able to capture the lowered inhibition of O adsorption with temperature.

Snabl et al. reported defect-site diffusion observed for CO on Pd (1 1 1) with the diffusion coefficient increasing with temperature (Snabl et al., 1997). Kaukonen et al. have also reported in their MC simulation of CO oxidation on platinum group metals that CO diffusion on the surface improves reactivity through avoiding formation of CO clusters (Kaukonen and Nieminen, 1989). Both these studies also confirm that the O adsorption inhibition is reduced with temperature. Thus, it is justified to add a parameter which accounts for the temperature dependence of the O coverage.

There have been multiple values of activation energy reported for CO oxidation on Pd depending on the crystal structure or support. Multiple studies have reported activation barriers for this reaction under UHV conditions (Engel and Ertl, 1978; Engel and Ertl, 1979; Berlowitz et al., 1988; Hendriksen, 2004; Gao et al., 2009; Stuve et al., 1984; Szanyi and Goodman, 1994; Zheng and Altman, 2002; Goodman, 1995; Nakao et al., 2006), near atmospheric conditions (Blomberg et al., 2016; Bunluesin et al., 1996) or even low pressure conditions (Conrad et al., 1978; Guo and Yates, 1989; Guo et al., 1989; Matsushima and White, 1975; Matsushima et al., 1975). Some of these studies have focused on only one crystal plane. A DFT study by Hammer has also provided E_A values at step or edge sites of the Pd structure (Hammer, 2001). Polycrystallinity has been observed in the particles embedded in the chip (Alekseeva et al., 2017). Fig. 11 shows some of the data

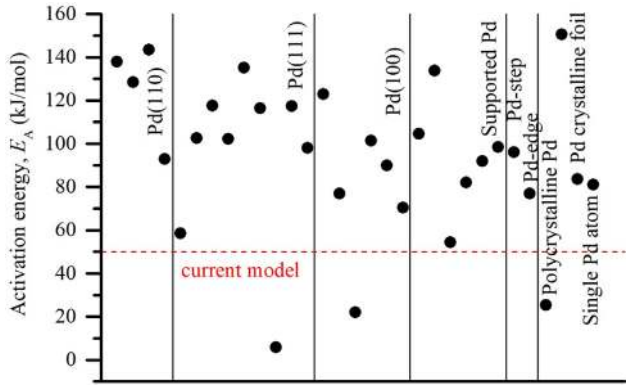

Fig. 11. Reaction activation barrier of CO oxidation on Palladium found in literature (Engel and Ertl, 1978; Engel and Ertl, 1978; Conrad et al., 1978; Berlowitz et al., 1988; Creighton et al., 1981; Gao et al., 2009; Szanyi and Goodman, 1994; Zheng and Altman, 2002; Goodman, 1995; Nakao et al., 2006; Bunluesin et al., 1996; Matsushima and White, 1975; Matsushima et al., 1975; Hammer, 2001; Salo et al., 2002; Eichler, 2002; Abbet et al., 2001; Turner et al., 1981; Piccinin and Stamatakis, 2014; Zhang and Hu, 2001; Liu and Evans, 2006; Eriksson and Ekedahl, 1998; Ehsasi et al., 1989; Bekyarova et al., 1998; Choi and Vannice, 1991; Coulston and Haller, 1991).

on E_A obtained from literature. The predicted E_A values compare well to the values observed in literature for polycrystalline Pd. Various facets are made available during the manufacturing which in turn reduces the reaction activation energy. The algorithms used here are crude approximations of models proposed by Engel and Ertl, Kisliuk and Polanyi and Wigner (Engel and Ertl, 1978; Kisliuk, 1958; Kolasinski, 2012). The adsorption mechanisms always suggest a co-adsorption behavior of CO and O. Thus, in this work, an effort has been made to manipulate behavior related to surface coverages and observe effects on the resulting CO_2 production.

Along with the nature of the surface, the DSMC simulation has also provided deeper insights into the reactor. Kinetic data can be extracted from each individual Pd particle in the nanochannel. In Fig. 12, the average local reaction rate on the particles is shown at the same gas composition, 0.8% CO and 6% O_2 (v/v) at three different temperatures. The CO_2 concentration is shown in both Fig. 9 and with an additional parameter k_{CO} in Fig. 10. At a temperature of 498 K, the reaction front is pushed towards the outlet showing how the reactor system has been poisoned. It also suggests that increasing the CO concentration the reaction rate will only decrease further. On the other hand, at 548 K the maximum reaction rate is observed closer to the inlet. This demonstrates that reactor is still active and that the CO_2 production is kinetically controlled. It is noted, however, that the particles downstream the zone of high local reaction rate have a low CO concentration and thus operate in a mass-transfer limited regime.

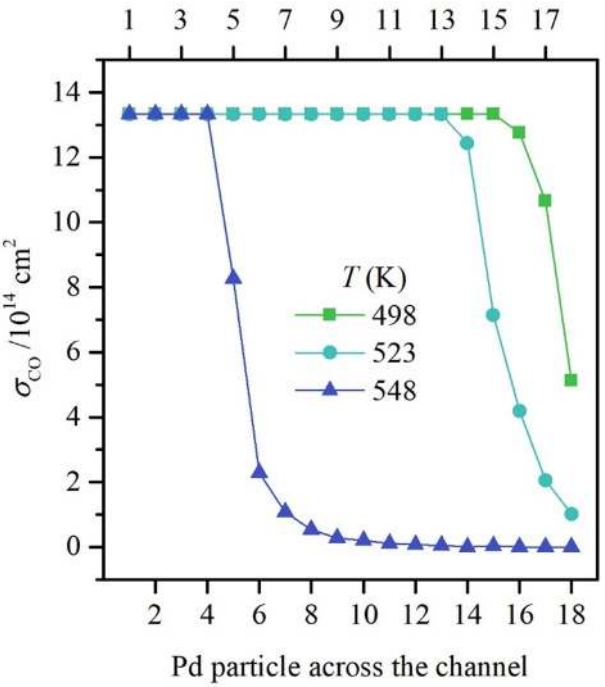

Fig. 13. Average local CO coverage on each Pd particle. The temperature is increased and the feed composiiton is fixed at 0.8% CO and 6% O_2. Comparing this figure with Fig. 16, the reaction rate is zero where the CO coverage is maximum. In other words, the surface is fully poisoned there by CO.

Along with the local reaction rate, the local CO coverage for the same conditions is presented in Fig. 13. The surface shows a maximum CO coverage for the particles that show low/zero reaction rate in Fig. 12. This clearly illustrates the CO poisoning behavior mentioned before. The reactor is almost poisoned at 498 K whereas at 548 K the reactor is still active.

The local CO coverage can be resolved into even higher resolution. In Fig. 14, the CO coverage is shown at a cellular resolution at

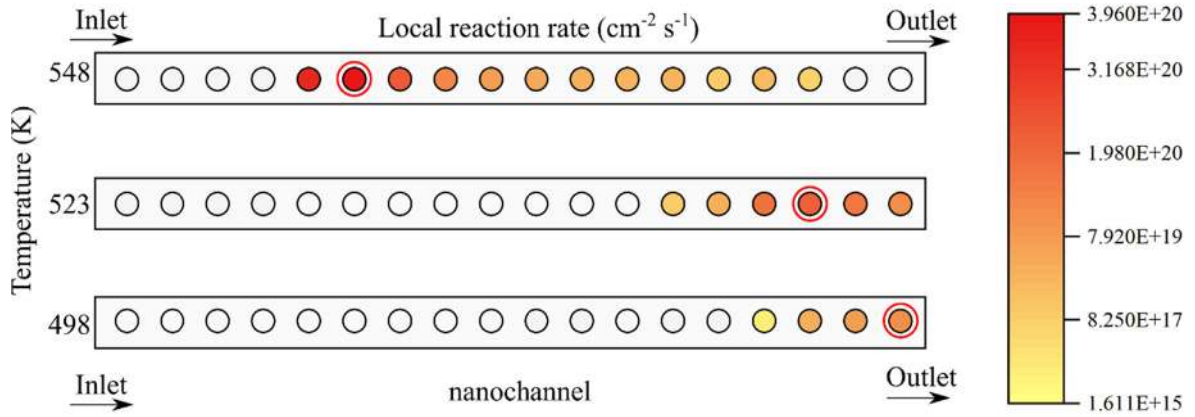

Fig. 12. Local reaction rate across the Pd particles in the nanochannel. The CO concentration is fixed at 0.8 vol%. The particle with the highest reaction rate at each temperature is marked with a surrounding red circle. The maximum reaction rate is higher at higher temperature. The reaction front has shifted towards the inlet as the temperature increases. This suggests that with a CO concentration of 0.8%, the reactor is close to being fully poisoned at 498 K. (For interpretation of the references to colour in this figure legend, the reader is referred to the web version of this article.)

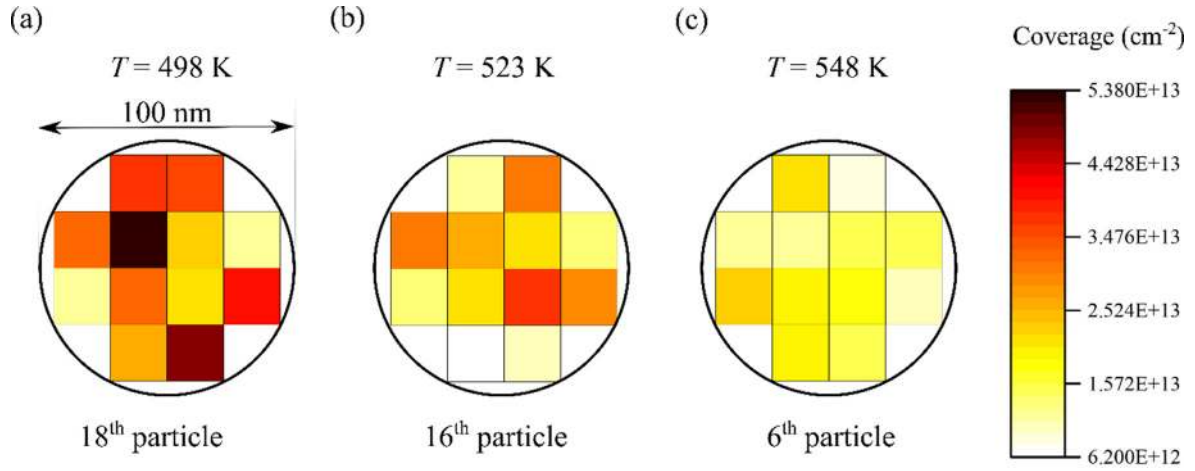

Fig. 14. Local CO coverage (in cm^{-2}) on the particle as the CO inlet concentration is 6%. As the temperature increases, the reaction rate increases and the corresponding CO coverage is lower as the adsorbed CO reacts off. The Pd particles shown in (a), (b) and (c) correspond to the maximum reaction rate found for each temperature in Fig. 12. The gas flow is from left to right. Note that the particles are located at different positions in the channel. The Pd particle shown in (a) is close to getting fully poisoned whereas the one shown in (c) is still active.

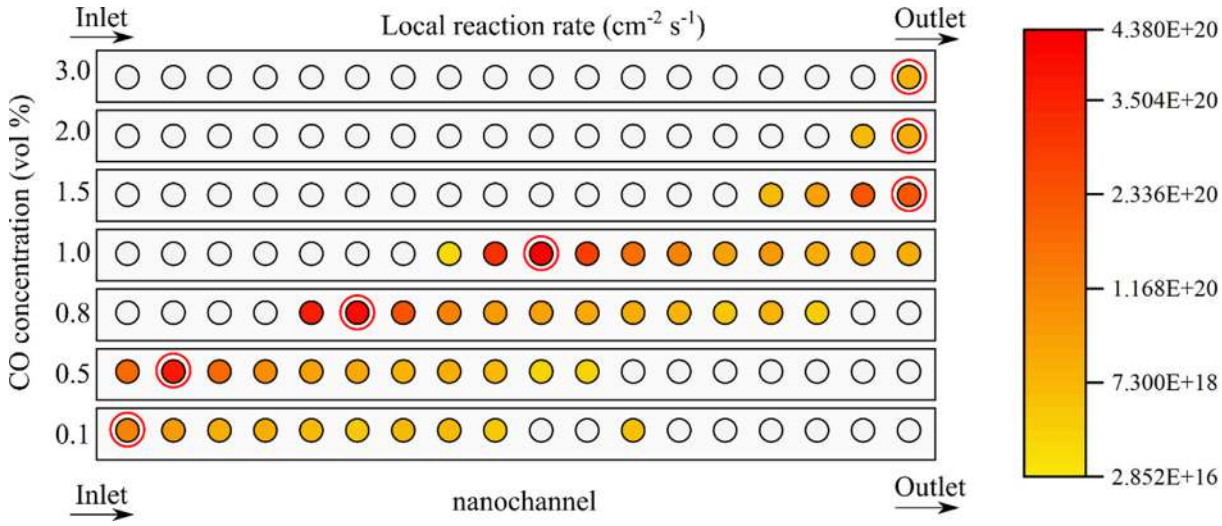

Fig. 15. Local reaction rate across the Pd particles in the nano channel. The temperature is constant at 548 K. The CO concentration is varied. The maximum reaction rate is marked by a surrounding red circle. The reaction front has shifted towards the outlet as the CO concentration increases, proving once again that excess CO poisons the surface. (For interpretation of the references to colour in this figure legend, the reader is referred to the web version of this article.)

the steady state. At a CO concentration of 8 vol%, the CO coverage is higher for T = 498 K compared to 548 K. With a lower reaction rate at a lower temperature, the Pd particle shown in Fig. 14(a), has a high CO coverage. It inhibits the adsorption of O and correspondingly the reaction rate decreases as seen in Fig. 14. The opposite is true for Fig. 14(c). As temperature increases, the CO poisoning is reduced due to increased desorption and thus the reaction rate increases. With such kind of analysis, one can address enhanced reactivity at sites of defects or kinks in the lattice.

Similar analysis is done for different CO concentrations at a constant temperature in Figs. 15 and 16. Keeping the temperature constant at 548 K, the CO concentration is varied from 0.1% to 3.0%. In analogy with previous analysis, the reaction front moves from the inlet to the outlet as the concentration is increased. The resulting CO_2 concentration first increases with increasing CO concentration and then reduces due to CO surface poisoning. Thus, a peak is noticed in Fig. 10. The mass transfer-limited regime is replaced by a kinetic-limited regime as the CO concentration is increased. For Fig. 16, an increase in CO concentration leads to an increase in adsorbed CO. An increase in adsorbed CO also means onset of inhibition of O. Thus, a proper CO concentration needs to be chosen such that the adsorbed CO can react off faster and not inhibit O adsorption.

In Fig. 17, the local gas phase concentration is shown. The parameters for this particular figure are: T = 548 K, CO_{inlet} = 0.8% and O_{inlet} = 6%. The time step shown here is after steady state has been achieved. The CO molecules are adsorbed in the first few Pd particles and thus the gas phase concentration drops to zero.

Thus, it is shown here how DSMC is a powerful package for prediction of local coverages and kinetics while also solving mass flow at a reactor scale. With this parcel simulation method, temporal and spatial discretization can be achieved for reacting rarefied gas flows, such as those in porous media.

5. Conclusions

With the help of a DSMC simulation extended for surface reaction, it was possible to obtain deeper insights into the chemical

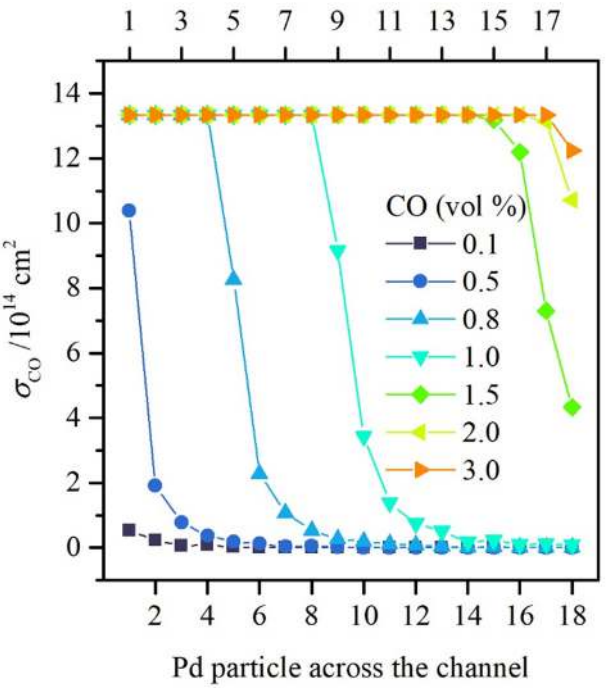

Fig. 16. Average local CO coverage on each Pd particle as the CO concentration is increased keeping the temperature constant at 548 K.

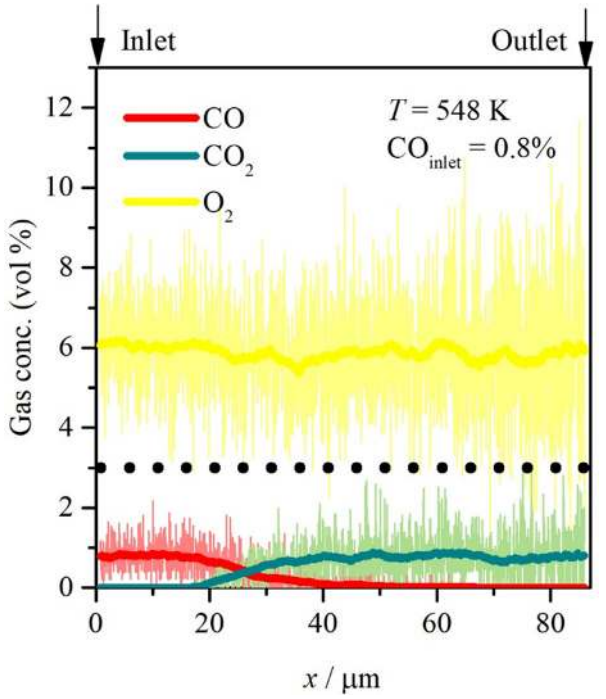

Fig. 17. Gas phase concentration in the channel at steady state. The temperature is 548 K and the inlet gas composition is CO:O_2:Ar = 1:6:93. Ar concentration is not shown here. The black circles refer to the position of the Pd particles in the nanochannel.

kinetics of CO oxidation on Pd particles in nanofluidic channels in an in-house manufactured chip. The simulation is able to provide specific particle local coverage and reaction rate data. Along with that, the overall channel CO_2 prediction by the simulation matches with those of experiment. Thus, the simulation is able to capture local insights while being uniquely able to describe the complete reactor system used in the experiment without compromising with the generally accepted mechanisms. The DSMC model developed in this paper is phenomenological and is a crude mean field approximation of the crystal surface. Defects, steps or any other crystal irregularities have been neglected from the modeling. With the benefit of a shorter simulation time, these mean-field simulations provide comprehension into the complicated elementary mechanisms of surface reactions at much reduced cost compared to other elaborate methods such as DFT or MD. The presented algorithm has proven suitable to predict microscopic data and also compute macroscopic transport properties in a reasonable time. Such detailed analysis could assist in optimization of reactor structures to improve catalytic performance and reduce manufacturing costs.

CRediT authorship contribution statement

Sangita Swapnasrita: Writing - Original draft, Methodology, Software, Validation, Formal analysis. **David Albinsson:** Methodology, Validation, Investigation. **Georg R. Pesch:** Writing - review & editing, Methodology, Software. **Henrik Ström:** Supervision, Funding acquisition, Writing - review & editing. **Christoph Langhammer:** Resources, Supervision, Funding acquisition, Writing - review & editing, Project administration. **Lutz Mädler:** Resources, Supervision, Funding acquisition, Writing - review & editing, Project administration.

Declaration of Competing Interest

The authors declare that they have no known competing financial interests or personal relationships that could have appeared to influence the work reported in this paper.

Acknowledgements

The financial support was provided by the German Science Foundation under the Leibniz Program (Grant MA 3333/13-1) and German Research Foundation (DFG) through the Research Training Group 1860 "Micro-,meso- and macroporous nonmetallic Materials: Fundamentals and Applications" (MIMENIMA). We would also like to thank MIMENIMA for providing the computational infrastructure for this work. This research has also received funding from the European Research Council (ERC) under the European Union's Horizon 2020 research and innovation programme (678941/SINCAT) and from the Knut and Alice Wallenberg Foundation project 2015.0055. Henrik Ström acknowledges funding from the Swedish Energy Agency (P34721-3).

Appendix A. Supplementary data

Supplementary data to this article can be found online at https://doi.org/10.1016/j.cesx.2021.100088.

References

Deutschmann, O., 2012. Modeling and simulation of heterogeneous catalytic reactions: from the molecular process to the technical system. Wiley-VCH Verlag & Co KGaA, Germany.
Andersen, M., Panosetti, C., Reuter, K., 2019. A Practical Guide to Surface Kinetic Monte Carlo Simulations. Frontiers in Chemistry. 7, 202. https://doi.org/10.3389/fchem.2019.00202.
Alexander, F.J., Garcia, A.L., 1997. The direct simulation Monte Carlo method. Computers in Physics. 11 (6), 588–593. https://doi.org/10.1063/1.168619.
Gimelshein, S., Wysong, I., 2017. DSMC modeling of flows with recombination reactions. Physics of Fluids. 29, (6). https://doi.org/10.1063/1.4986529 067106.
Bird, G.A., 2011. Chemical Reactions in DSMC. AIP Conference Proceedings. 1333 (1), 1195–1202. https://doi.org/10.1063/1.3562806.
Dreyer, J.A.H., Riefler, N., Pesch, G.R., Karamehmedovic, M., Fritsching, U., Teoh, W. Y., Mädler, L., 2014. Simulation of gas diffusion in highly porous nanostructures

by direct simulation Monte Carlo. Chemical Engineering Science. 105, 69–76. https://doi.org/10.1016/j.ces.2013.10.038.
Pesch, G.R., Riefler, N., Fritsching, U., Ciacchi, C., Mädler, L., 2015. Gas-solid catalytic reactions with an extended DSMC model. AIChE Journal. 61 (7), 2092–2103. https://doi.org/10.1002/aic.14856.
Swapnasrita, S., Pesch, G.R., Dreyer, J.A.H., Riefler, N., Wriedt, T., Mädler, L., 2019. Implementation of parcel method for surface reactions in DSMC. Computers & Fluids. 187, 1–11. https://doi.org/10.1016/j.compfluid.2019.04.015.
Rogal, J., Reuter, K., Scheffler, M., 2007. CO oxidation at Pd(100): A first-principles constrained thermodynamics study. Physical Review B 75, (20). https://doi.org/10.1103/PhysRevB.75.205433 205433.
Pan, T.J., Wilson, T.J., Stephani, K.A., 2019. Vibrational state-specific model for dissociation and recombination of the O2(3Σg−)+O(3P) system in DSMC. The Journal of Chemical Physics 150, (7). https://doi.org/10.1063/1.5035283 074305.
Swaminathan-Gopalan, K., Borner, A., Murray, V.J., Poovathingal, S., Minton, T.K., Mansour, N.N., Stephani, K.A., 2018. Development and validation of a finite-rate model for carbon oxidation by atomic oxygen. Carbon 137, 313–332. https://doi.org/10.1016/j.carbon.2018.04.088.
Swaminathan-Gopalan, K., Stephani, K.A., 2019. Construction of finite rate surface chemistry models from pulsed hyperthermal beam experimental data. AIP Advances 9, (3). https://doi.org/10.1063/1.5082553 035246.
Albinsson, D., Bartling, S., Nilsson, S., Ström, H., Fritzsche, J., Langhammer, C., 2020. Operando detection of single nanoparticle activity dynamics inside a model pore catalyst material. Science. Advances. 6 (25), eaba7678. https://doi.org/10.1126/sciadv.aba7678.
Alekseeva, S., Fanta, A.Bd.S., Iandolo, B., Antosiewicz, T.J., Nugroho, F.A.A., Wagner, J. B., Burrows, A., Zhdanov, V.P., Langhammer, C., 2017. *Grain boundary mediated hydriding phase transformations in individual polycrystalline metal nanoparticles.* nature. Communications. 8 (1), 1–10. https://doi.org/10.1038/s41467-017-00879-9.
Scanlon, T.J. et al., 2010. An open source, parallel DSMC code for rarefied gas flows in arbitrary geometries. Computers & Fluids 39 (10), 2078–2089. https://doi.org/10.1016/j.compfluid.2010.07.014.
Roohi, E., Stefanov, S., 2016. Collision partner selection schemes in DSMC: From micro/nano flows to hypersonic flows. Physics Reports 656, 1–38. https://doi.org/10.1016/j.physrep.2016.08.002.
Engel, T., Ertl, G., 1978. A molecular beam investigation of the catalytic oxidation of CO on Pd (111). The Journal of Chemical Physics. 69 (3), 1267–1281. https://doi.org/10.1063/1.436666.
Koura, K., Matsumoto, H., 1992. Variable soft sphere molecular model for air species. Physics of Fluids A: Fluid Dynamics. 4 (5), 1083–1085. https://doi.org/10.1063/1.858262.
Bird, G.A. and J.M. Brady, Molecular gas dynamics and the direct simulation of gas flows. Oxford: Clarendon press, Vol. 5. 1994.
Amiri-Jaghargh, A., Roohi, E., Stefanov, S., Nami, H., Niazmand, H., 2014. DSMC simulation of micro/nano flows using SBT–TAS technique. Computers & Fluids 102, 266–276. https://doi.org/10.1016/j.compfluid.2014.07.003.
Roohi, E., Stefanov, S., Shoja-Sani, A., Ejraei, H., 2018. A generalized form of the Bernoulli Trial collision scheme in DSMC: Derivation and evaluation. Journal of Computational Physics 354, 476–492. https://doi.org/10.1016/j.jcp.2017.10.033.
Kisliuk, P., 1957. The sticking probabilities of gases chemisorbed on the surfaces of solids. Journal of Physics and Chemistry of Solids. 3 (1), 95–101. https://doi.org/10.1016/0022-3697(57)90054-9.
Kisliuk, P., 1958. The sticking probabilities of gases chemisorbed on the surfaces of solids—II. Journal of Physics and Chemistry of Solids. 5 (1), 78–84. https://doi.org/10.1016/0022-3697(58)90132-X.
Kolasinski, K.W., 2012. *Surface Science: Fundamentals of catalysis and nanoscience* (3rd edition). John Wiley & Sons Ltd, United Kingdom.
Engel, T., Ertl, G., 1978. Surface residence times and reaction mechanism in the catalytic oxidation of CO on Pd(111). Chemical Physics Letters. 54 (1), 95–98. https://doi.org/10.1016/0009-2614(78)85673-5.
Engel, T., Ertl, G., 1979. Elementary Steps in the Catalytic Oxidation of Carbon Monoxide on Platinum Metals. Advances in Catalysis. 28, 1–78. https://doi.org/10.1016/S0360-0564(08)60133-9.
Conrad, H., Ertl, G., Küppers, J., 1978. Interactions between oxygen and carbon monoxide on a Pd(111) surface. Surface Science. 76 (2), 323–342. https://doi.org/10.1016/0039-6028(78)90101-2.
Berlowitz, P.J., Peden, C.H.F., Goodman, D.W., 1988. Kinetics of carbon monoxide oxidation on single-crystal palladium, platinum, and iridium. The Journal of Physical Chemistry. 92 (18), 5213–5221. https://doi.org/10.1021/j100329a030.
Hendriksen BLM, S.C. Bobaru SC, Frenken JWM. Oscillatory CO oxidation on Pd(100) studied with in situ scanning tunneling microscopy. Surface Science. 2004; 552 (1): 229-242. 10.1016/j.susc.2004.01.025
Guo, X., Yates, J.T., 1989. Dependence of effective desorption kinetic parameters on surface coverage and adsorption temperature: CO on Pd(111). The Journal of Chemical Physics. 90 (11), 6761–6766. https://doi.org/10.1063/1.456294.
Guo, X., Hoffman, A., Yates, J.T., 1989. Adsorption kinetics and isotopic equilibration of oxygen adsorbed on the Pd(111) surface. The Journal of Chemical Physics. 90 (10), 5787–5792. https://doi.org/10.1063/1.456386.
Creighton, J.R., Tseng, F.H., White, J.M., Turner, J.S., 1981. Numerical modeling of steady-state carbon monoxide oxidation on platinum and palladium. The Journal of Physical Chemistry. 85 (6), 703–708. https://doi.org/10.1021/j150606a019.
Snabl, M., Borusik, O., Chab, V., Ondrejcek, M., Stenzel, W., Conrad, H., Bradshaw, M., 1997. Surface diffusion of CO molecules on Pd(111) studied with photoelectron emission microscopy. Surface Science. 385 (2), L1016–L1022. https://doi.org/10.1016/S0039-6028(97)00435-4.
Kaukonen, H.P., Nieminen, R.M., 1989. Computer simulations studies of the catalytic oxidation of carbon monoxide on platinum metals. The Journal of Chemical Physics. 91 (7), 4380–4386. https://doi.org/10.1063/1.456818.
Gao, F., Wang, Y., Cai, Y., Goodman, D.W., 2009. CO Oxidation on Pt-Group Metals from Ultrahigh Vacuum to Near Atmospheric Pressures. 2. Palladium and Platinum. The Journal of Physical Chemistry C. 113 (1), 174–181. https://doi.org/10.1021/jp8077985.
Stuve, E.M., Madix, R.J., Brundle, C.R., 1984. CO oxidation on Pd(100): A study of the coadsorption of oxygen and carbon monoxide. Surface Science. 146 (1), 155–178. https://doi.org/10.1016/0039-6028(84)90235-8.
Szanyi, J., Goodman, D.W., 1994. CO oxidation on palladium. 1. A combined kinetic-infrared reflection absorption spectroscopic study of Pd (100). The Journal of Physical Chemistry. 98 (11), 2972–2977. https://doi.org/10.1021/j100062a038.
Zheng, G., Altman, E.I., 2002. The Reactivity of Surface Oxygen Phases on Pd(100) Toward Reduction by CO. The Journal of Physical Chemistry B. 106 (5), 1048–1057. https://doi.org/10.1021/jp013395x.
Goodman, D.W., 1995. Model Studies in Catalysis Using Surface Science Probes. Chemical Reviews. 95 (3), 523–536. https://doi.org/10.1021/cr00035a004.
Nakao, K., Ito, S.I., Tomishige, K., Kunimori, K., 2006. Reaction mechanism and structure of activated complex of CO2 formation in CO oxidation on Pd(110) and Pd(111) surfaces. Catalysis Today. 111 (3), 316–321. https://doi.org/10.1016/j.cattod.2005.10.043.
Blomberg, S., Zetterberg, J., Gustafson, J., Zhou, J., Brackmann, C., Lundgren, E., 2016. Comparison of AP-XPS and PLIF Measurements During CO Oxidation Over Pd Single Crystals. Topics in Catalysis. 59 (5), 478–486. https://doi.org/10.1007/s11244-015-0524-4.
Bunluesin, T., Putna, E.S., Gorte, R.J., 1996. A comparison of CO oxidation on ceria-supported Pt, Pd, and Rh. Catalysis Letters. 41 (1), 1–5. https://doi.org/10.1007/BF00811703.
Matsushima, T., White, J.M., 1975. On the mechanism and kinetics of the CO-oxidation reaction on polycrystalline palladium: I. The reaction paths. Journal of Catalysis. 39 (2), 265–276. https://doi.org/10.1016/0021-9517(75)90331-0.
Matsushima, T., Almy, D.B., Foyt, D.C., Close, J.S., White, J.M., 1975. On the mechanism and kinetics of the CO-oxidation reaction on polycrystalline palladium: II. The kinetics. Journal of Catalysis. 39 (2), 277–285. https://doi.org/10.1016/0021-9517(75)90332-2.
Hammer, B., 2001. The NO+CO Reaction Catalyzed by Flat, Stepped, and Edged Pd Surfaces. Journal of Catalysis. 199 (2), 171–176. https://doi.org/10.1006/jcat.2000.3147.
Salo, P., Honkala, K., Alatalo, M., Laasonen, K., 2002. Catalytic oxidation of CO on Pd (111). Surface Science. 516 (3), 247–253. https://doi.org/10.1016/S0039-6028(02)01965-9.
Eichler, A., 2002. CO oxidation on transition metal surfaces: reaction rates from first principles. Surface Science. 498 (3), 314–320. https://doi.org/10.1016/S0039-6028(01)01805-2.
Abbet, S., Heiz, U., Häkkinen, H., Landman, U., 2001. CO Oxidation on a Single Pd Atom Supported on Magnesia. Physical Review Letters. 86 (26), 5950–5953. https://doi.org/10.1103/PhysRevLett.86.5950.
Turner JE, Sales BC, Maple MB. Oscillatory oxidation of CO over Pd and Ir catalysts. Surface Science. 1981; 109(3): 591-604. 0.1016/0039-6028(81)90429-5
Piccinin, S., Stamatakis, M., 2014. CO Oxidation on Pd(111): A First-Principles-Based Kinetic Monte Carlo Study. ACS Catalysis. 4 (7), 2143–2152. https://doi.org/10.1021/cs500377j.
Zhang, C.J., Hu, P., 2001. CO Oxidation on Pd(100) and Pd(111): A Comparative Study of Reaction Pathways and Reactivity at Low and Medium Coverages. Journal of the American Chemical Society. 123 (6), 1166–1172. https://doi.org/10.1021/ja002432f.
Liu, D.J., Evans, J.W., 2006. Atomistic lattice-gas modeling of CO oxidation on Pd (100): Temperature-programed spectroscopy and steady-state behavior. The Journal of Chemical Physics. 124, (15). https://doi.org/10.1063/1.2186314 154705.
Eriksson, M., Ekedahl, L.G., 1998. The catalytic oxidation of CO on polycrystalline Pd: experiments and kinetic modeling. Surface Science. 412–413, 430–440. https://doi.org/10.1016/S0039-6028(98)00462-2.
Ehsasi, M., Seidel, C., Ruppender, H., Drachsel, W., Block, J.H., Christmann, K., 1989. Kinetic oscillations in the rate of CO oxidation on Pd(110). Surface Science Letters. 210 (3), L198–L208. https://doi.org/10.1016/0167-2584(89)90803-7.
Bekyarova, E., Fornasiero, P., Kaspar, J., Graziani, M., 1998. CO oxidation on Pd/CeO2–ZrO2 catalysts. Catalysis Today. 45 (1), 179–183. https://doi.org/10.1016/S0920-5861(98)00212-0.
Choi, K.I., Vannice, M.A., 1991. CO oxidation over Pd and Cu catalysts IV. Prereduced Al2O3-supported copper. Journal of Catalysis. 131 (1), 22–35. https://doi.org/10.1016/0021-9517(91)90320-4.
Coulston, G.W., Haller, G.L., 1991. The dynamics of CO oxidation on Pd, Rh, and Pt studied by high-resolution infrared chemiluminescence spectroscopy. The Journal of Chemical Physics. 95 (9), 6932–6944. https://doi.org/10.1063/1.461505.